Optical Performance of Split-Source Z-Shaped Horizontal-Pocket and Hetero-Stacked TFET-Based Photosensors

Shreyas Tiwari[1] · Rajesh Saha[1]

Abstract

This paper compares the optical performance of a split-source horizontal-pocket Z-shaped tunnel field-effect transistor (ZHP-TFET) and hetero-stacked TFET (HS-TFET) using a technology computer-aided design simulator. The optical analysis supports the application of TFETs as photosensors or photodiodes. Variation in optical behavior is observed under light and dark conditions. The performance parameters of the proposed devices including energy band diagram, electrostatic potential, band-to band-tunneling rate, and electron density are compared under both light and dark conditions. The effect of strain on the HS-TFET due to the heterojunction source is also investigated. Additionally, the spectral sensitivity (S_n), responsivity (R), and signal-to-noise ratio (SNR) for these photodiodes are reported. The ZHP-based TFET photodiode provides an SNR value of 44 dB and responsivity of 0.17 (A/W), whereas the HS-TFET-based photodiode exhibits SNR of 78 dB and responsivity of 0.04 (A/W). The results reveal that the responsivity (R) and quantum efficiency (η) of the ZHP-based TFET photodiode are significantly higher than those of the HS-TFET-based photodiode. Also, a greater improvement in SNR and spectral sensitivity is observed in the HS-TFET photodiode than the ZHP-TFET photodiode. Finally, a comparative study of optical parameters between the ZHP-TFET and HS-TFET photodiodes is highlighted.

Keywords Current spectral density · hetero-stack · horizontal pocket · TFET

Introduction

The semiconductor industry has identified the metal–oxide–semiconductor field-effect transistor (MOSFET) as a basic element for device-, circuit-, and system-level applications. Downscaling in MOSFET technology has many advantages, notably better radio-frequency (RF) performance, lower power consumption, and increased marginal density. Despite these advantages, however, constant MOSFET downscaling has numerous shortcomings, including a subthreshold swing (SS) limit of 60 mV/decade, substantial low-power dissipation, greater conduction losses, and massive short-channel effects (SCEs).[1–3] Tunnel field-effect transistors (TFETs) have been proposed as a potential replacement for MOSFETs, as well as a basis for future semiconductor technologies.[2] TFETs have unique features that make them ideal for a variety of applications, including low-power, analog/RF, and optical sensing.[4,5] On the other hand, TFETs have some challenges, including larger ambipolar[6–11] conduction, low ON-state current, and poor high-frequency performance.[12] To overcome these problems, the line TFET has been emphasized in the literature by researchers.[13] In a line TFET, an oxide and gate material is placed over the source region, which leads to activation of the vertical electrical field component and induced orthogonal to the source area.[14] This vertical electric field component over the gate terminal enhances the tunneling phenomena of the device. Subsequently, it also plays an important role in enhancing the quantum tunneling mechanism, degrading the ambipolar conduction, and enabling the device to switch quickly comparatively to conventional TFET devices. To further improve the performance of the line TFET, a Z-shaped horizontal pocket (ZHP) line TFET[15–18] is designed to achieve high drain current and low leakage current. In this structure, the n^+ pocket is placed over the p^+ source area, resulting in a Z-shaped oxide layer with a horizontal pocket. In the

✉ Rajesh Saha
rajeshsaha93@gmail.com

Shreyas Tiwari
shreyastiwari21@gmail.com

[1] Department of Electronics and Communication Engineering, Malaviya National Institute of Technology Jaipur, Jaipur, Rajasthan 302017, India

ZHP-TFET, a hafnium dioxide (HfO_2) layer is placed over the source area, while a thin film of silicon dioxide (SiO_2) is kept beneath the channel region. Agopin et al. experimentally highlighted the electrical characteristics of the line TFET.[13] Analysis revealed that the Z-TFET has improved transfer characteristics, current ratio, and RF/analog performance than double-gate TFETs (DG-TFETs) even in the presence of traps.[19] It was also observed that the ZHP-TFET has better transfer characteristics, I_{ON}/I_{OFF} ratio, I_{ON}/I_{AMB} ratio, SS, and RF/analog performance than the Z-TFET and DG-TFET.[20] To reduce the ambipolar current and improve ON current, a split-drain Z-shaped horizontal pocket (HP) TFET was proposed in the literature.[17] Furthermore, the performance of a Z-shaped charge plasma TFET as a biosensor was analyzed considering different biomolecules inside the cavity by Shivangi et al.[21]

The hetero-stacked (HS)[22,23] TFET is another fascinating device that divides the source into two sections: the top portion is composed of silicon, and the lower section is made of germanium. These hetero-structural modifications lead to a reduction in ambipolar conduction, improvement in steepness of the SS, and reduced leakage current.

The main objective of the present work is to examine the optical performance of low-power hetero-stacked and Z-shaped horizontal-pocket TFETs in the visible range of the spectrum (400–700) nm at an intensity of 0.7 W/cm². Various optical figures of merit (FOMs) including spectral sensitivity (S_n), quantum efficiency (η), signal-to-noise ratio (SNR), and responsivity (R) are key parameters for determining the optical performance of these TFET-based photosensors. When light strikes the device's sensitive portion, photons are absorbed, resulting in the formation of optical charge carriers within the illumination window.[24,25] Furthermore, significant changes in their optical properties[26–28] have been detected when the intensity and wavelength[23] of incident light are varied. The stress distribution of the HS-TFET is also emphasized for more practical and realistic analysis.

Moreover, the fabrication process flow for both structures is also presented.

This paper is organized in four sections. Section "Device Structure and Simulation Setup" includes the device structure and simulation parameters followed by the fabrication process flow for these TFETs, with an explanation of how it can function as a photodiode, Section "Results and Discussion" examines the optical properties of these TFET-based photodiodes. Finally, Sect. "Conclusion" concludes the paper.

Device Structure and Simulation Setup

The Z-shaped horizontal-pocket (ZHP) TFET and hetero-stacked (HS) TFET photodiodes considered in this work are presented in Fig. 1a and b, and their various parameters are defined from the existing literature.[15–23] Table I shows the device dimensions and doping specifications for both devices. The gate and source regions of the ZHP-TFET (Fig. 1a) have 1 nm-thick layers of SiO_2 and HfO_2 layers, respectively. In addition, a 3 nm-thick n^+ pocket is placed over the source to improve the tunneling rate and exhibits the maximum photon absorption. Furthermore, the ZHP-TFET aids in the reduction of undesired interface trap charges beneath the oxide layer and leads to minimum changes in drain current (I_D) during the illumination state. The HS-TFET shown in Fig. 1b is composed of a stack source region with two distinct semiconductor materials: the upper layer employs Si, while the lower layer features Ge.

The lower bandgap of Ge than of Si leads to the improved effective switching characteristics,[18] and thus, the HS-TFET has a steeper average SS. To examine the effects of optical phenomena, the light should be incident on the gate section of the device. The stepwise fabrication process flow for the ZHP- and HS-TFET-based photodiodes is summarized in Fig. 2a and b, respectively. Thus, the exploration of the
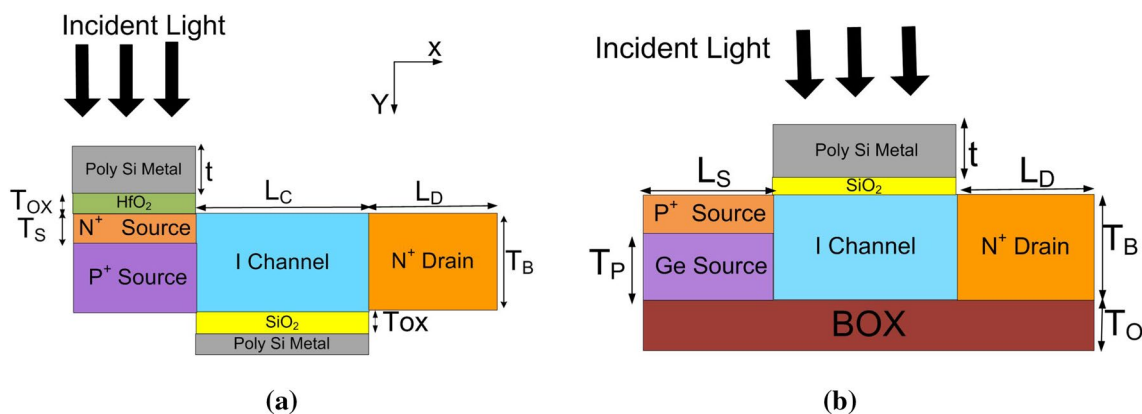

Fig. 1 Two-dimensional schematic of (a) ZHP-TFET and (b) HS-TFET photodiodes.

Table I Device parameters of the considered photodiodes

Parameters	Values
Channel length (L_c)	30 nm
SiO$_2$ thickness (T_{OX})	1 nm
HfO$_2$ thickness (T_{OX})	1 nm
Length of pocket (L_S)	30 nm
Photosensitive metal thickness (t)	35 nm
N$^+$ pocket thickness (T_S)	3 nm
Body thickness (T_B)	10 nm
Ge source thickness (T_P)	5 nm
Buried oxide (BOX) thickness (T_O)	5 nm
Source pocket doping (n-type)	1×10^{19} cm^{-3}
Channel doping	1×10^{15} cm^{-3}
Drain doping (n-type)	5×10^{18} cm^{-3}
Source doping (p-type)	1×10^{20} cm^{-3}
HfO$_2$ dielectric constant	24
Tunnel gate work function	4.32 eV
Source length (L_S)	30 nm
Drain length (L_D)	30 nm

TFET-based photodiode is not limited to simulation, and actual fabrication of such optical devices is also possible in the near future.

The process can be described as follows. Initially, we take an ideal Si substrate of required dimensions. The device area is defined through cutting edge technology of the wafer forming. Once the device area is defined, photo-masking with lithography[11] is used to deposit the *n*- and *p*-type dopants of uniform mode into the source and drain side of the device through a spin-on-dopant (SOD) process. In this technique, the dopant is first spread onto the substrate, and then diffusion takes place by a rapid thermal annealing process. This process of doping has been found very promising for ease of implementation, lower cost, and less crystal damage with uniform doping. In the next step, RCA cleaning of wafers is performed to remove contaminants. Afterwards, an oxide layer is deposited across the source, channel, and drain regions by atomic layer deposition (ALD). Selective etching of hafnium and silicon oxide is also performed using a dry reaction ion etching (RIE) and coupled plasma technique, and deposition of metal over the junction is carried out by electron beam evaporation. Finally, post-metallization
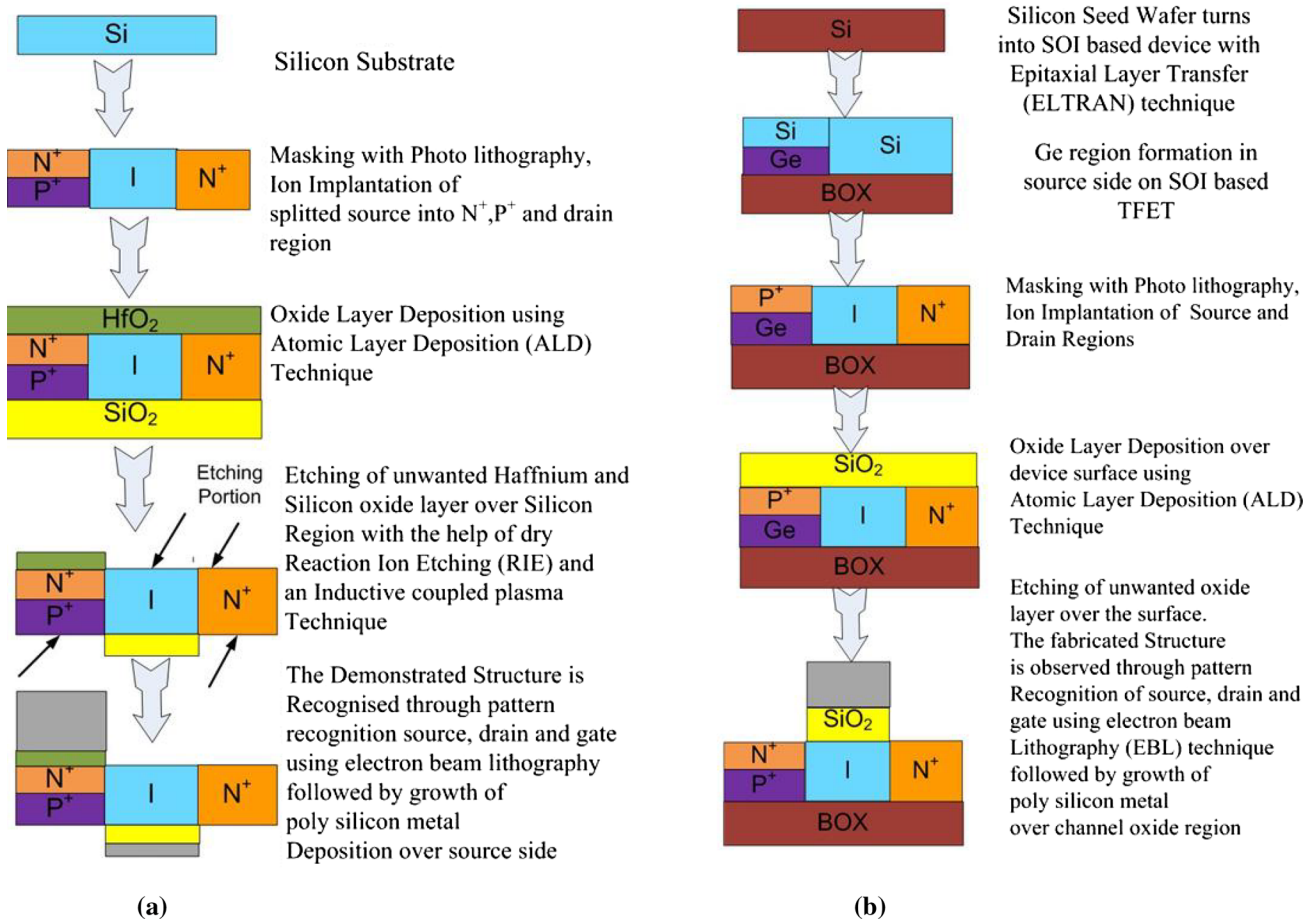
Fig. 2 Fabrication process steps for (a) ZHP-TFET and (b) HS-TFET photodiodes.

is used to tighten the connection between metal and silicon material.

The Sentaurus TCAD[29] tool is used to design these TFET-based photodiodes. The accuracy of the models is verified by comparison of experimental data with the simulation results.[30] The presence of highly doped source and drain regions leads to activation of the Fermi distribution model during simulation. To incorporate the recombination model in the simulator, the Shockley–Read–Hall (SRH) model is enabled. The bandgap narrowing slotboom model is activated, as the band-to-band tunneling (BTBT) rate is a function of the energy bandgap. The nonlocal BTBT model is commonly used to investigate carrier transport in such photodiodes. These models allow charge carriers to explore a tunneling path during the optical creation of carriers inside the illumination window. The indirect tunneling coefficients, $A = 3.29 \times 10^{15}$ cm^{-3} s^{-1}, $B = 23.8 \times 10^{6}$ Vcm^{-1} (for Si), and $A = 1.67 \times 10^{15}$ cm^{-3} s^{-1}, $B = 6.55 \times 10^{6}$ Vcm^{-1} (for Ge) are considered during calibration.[31] Noticeable matching is observed between the simulated and experimental data taken from Kim et al.,[30] as shown in Fig. 3.

Since there is no possibility of a depletion zone forming on the remaining structure, the "illumination window" of the device must display the depletion region for the device to function as a photodiode. It is reported in the literature that the TFET-based photodiode[25,32,33] has improved optical properties in the visible range of the spectrum due to its maximum optical absorbance in this wavelength range. This also ensures that incident light energy is greater than the threshold energy of material for generation of electron–hole pairs inside the photosensitive region of the device at constant intensity of light. Since the intensity of light may vary from 0.5 W/cm^2 to 0.7 W/cm^2 depending upon the optical properties and photosensitivity of the material,[32] and the proposed device displays exceptional variation at constant $I = 0.7$ W/cm^2 during optical simulation, the proposed photodiodes are simulated under a visible wavelength range of
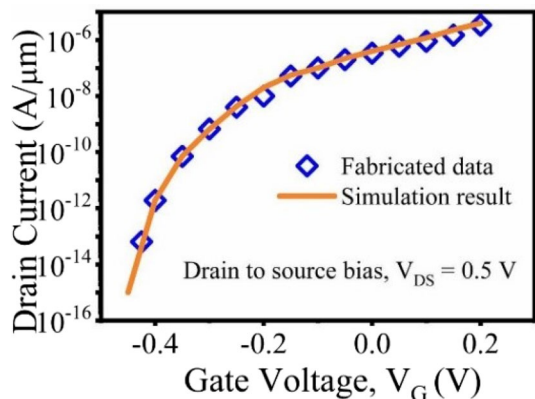
400–700 nm at constant intensity of 0.7 W/cm^2. In order to realize these TFETs as optical sensors, we defined a specific value of wavelength with its angle of incidence in the TCAD simulator.[29] The value of intensity and the dimensions of the illumination window over which optical operation will take place are also defined during simulation.

Strain will exist in the HS-TFET as Ge material is placed over Si. This strain analysis is realized in the simulator by activating the deformation mobility model, multi-valley electron mobility model, and piezoresistance mobility model.[29]

Results and Discussion

Figure 4 shows that the optical generation rate of the ZHP-TFET-based photodiode is higher than that of the HS-TFET photodiode. In a TFET, one challenge that remains is that ON current is observed in the range of microamperes. Thus, to realize high drain current, it is essential to increase the carrier transmission probability through an inter-band tunneling barrier. This tunneling barrier is defined through the Wentzel–Kramers–Brillouin (WKB) approximation (T_{wkb})[6] and mathematically expressed as

$$T_{wkb} = \exp\left[\frac{4\lambda\sqrt{2m^* E_g^3}}{3qh(E_q + \Delta\emptyset)}\right] \qquad (1)$$

where m^* is defined as the effective mass, E_g is the bandgap, λ is the tunneling length, q is the electronic charge, h is the Planck constant, and $\Delta\phi$ represents the energy difference between the valence and conduction energy bands. Here, m^* and E_g depend upon the material system properties, while
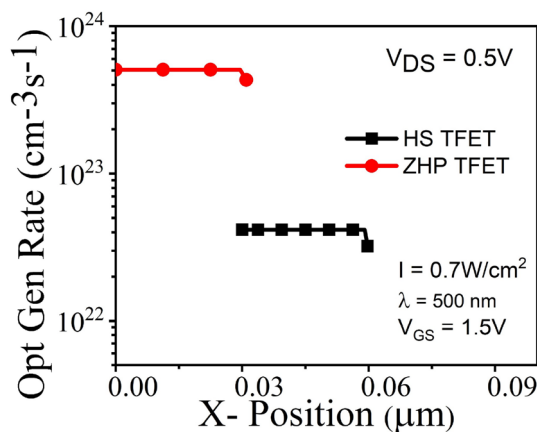

Fig. 3 Comparison of fabricated data from Kim et al.[30]

Fig. 4 Optical generation rate of HS- and ZHP TFET-based photodiodes at $\lambda = 500$ nm, $I = 0.7$ W/cm^2 at $V_{GS} = 1.5$ V.

for a smaller tunneling length (λ), better modulation of the device channel is desirable. Thus, it is desirable to considered a high-permittivity (high-k) oxide layer for better ON current and fast switching. Therefore, the availability of the HfO$_2$ layer over the source region in the ZHP-TFET results in greater confinement in the energy bands under the illumination state. Thus, the high-k oxide layer of HfO$_2$ is responsible for excess electron–hole pair generation when light of intensity 0.7 W/cm^2 in the visible range (0.3–0.7 μm) is incident over the photosensitive metal gate region of the device. Therefore, the higher dielectric constant of HfO$_2$ is responsible for excess drain current in the ZHP-TFET-based photodiode. As a result, the overall net optical generation rate in the ZHP-TFET photodiode is higher than that of the HS-TFET photodiode, as shown in Fig. 4.

Light is incident over the photosensitive poly-silicon metal[11,33] of thickness (t) in the gate region through the optical illumination window, as shown in Fig. 1a and b. When light is incident over the sensitive material, then a photochemical reaction is initiated by absorption of energy in the light form. Consequently, molecules absorbing the light are responsible for the generation of transient excited states whose chemical and physical properties are far different from the original molecules. These newly generated chemical molecules can play an important role in changing structures, can combine to form new molecules, and may possibly transfer electrons, hydrogen atoms, or their excited electronic energy to other molecules.[28] If a light wave of a certain frequency strikes a photosensitive material with electrons moving at the same vibrational frequency, then such electrons will absorb the light wave energy and convert it into a vibrational motion of light. During vibrational motion, the electrons interact with neighboring atoms, and consequently, their vibrational energy is transformed into the thermal energy of the material. These energy transformation phenomena are responsible for optical generation of charge carriers over the photosensitive region of an optical device.[11,33]

Calculation of the optical generation rate (G) with variation in light intensity on the basis of metal thickness (t) of given photodiodes can be described through some basic carrier generated equations. The equilibrium electron and hole concentrations in the photosensitive region are expressed as[32,33]

$$n = n_o + \delta n(\lambda) \qquad p = p_o + \delta p(\lambda) \tag{2}$$

where n_o and p_o are the electron and hole concentrations, respectively, in an equilibrium state under the dark condition, and $\delta n(\lambda)$ and $\delta p(\lambda)$ are defined as the excess electron and hole concentrations, respectively, at 500 nm wavelength. In the ideal state, $\delta n(\lambda) = \delta p(\lambda)$, and therefore the hole concentration can be written as

$$p = p_o + \delta n(\lambda) \tag{3}$$

By considering the SRH recombination model mechanism in the ideal state condition, the number of optically generated carriers per unit volume is defined as[25,33]

$$\delta n(\lambda) = G\tau_n = \alpha\varphi\tau_n e^{-\alpha t} \tag{4}$$

where ϕ is the photon flux density, α signifies the absorption coefficient per unit length, and τ_n represents the electron lifetime. The expression for generation rate is given by[32]

$$G = \frac{I}{h\tau_c}\alpha e^{-\alpha t} \tag{5}$$

$$I = Io(\lambda)\left(1 - R_c\right) \tag{6}$$

where $I_o(\lambda)$ is the intensity of incident light pursuing wavelength λ, R_c indicates the reflection coefficient at the air–Si interface of the gate region, and h and τ_c represent the Planck constant and carrier lifetime, respectively. In this optical analysis, we are assuming that incoming light is totally absorbed in the photosensitive gate region of the device. Thus, the net expression of excess carrier concentration is expressed as

$$\Delta n(\lambda) = I_o\alpha(\lambda)\tau_n\frac{\lambda}{hc}\left(1 - R_c\right)e^{-\alpha(\lambda)t} \tag{7}$$

Equation 7 defines the net charge carrier generation rate (G) inside the illumination window as exponentially dependent upon the metal gate thickness t. Since we have assumed that the proposed TFET-based photodiode exhibits complete absorption of light, no reflection would occur at the back surface of the device.

Figure 5a and b depicts the energy band diagrams for the HS-TFET photodiode under illumination and dark conditions, respectively. Energy band diagrams for the ZHP-TFET photodiode under light and dark conditions are demonstrated in Fig. 5c and d, respectively. When gate voltage (V_{GS}) is applied, the number of photo-generated electrons decreases as the device approaches its positive gate voltage, and the holes accumulate at the gate oxide area of the photodiode. It can be seen from Fig. 5 that the electron quasi-Fermi level (E_{fn}) and hole quasi-Fermi level (E_{fp}) of the photodiodes are segregated due to the separation of charge carriers. This phenomenon creates an illumination window for these photodiodes. Furthermore, the separation of these Fermi energy levels causes a potential difference within the gate region of the photodiode, referred to as photo-voltage (V_{op}). The induced photo-voltage (V_{op}) is responsible for the enhancement in photo-current at the initial value of gate voltage (V_{GS}). Figure 5a and c reveals that the decoupling of E_{fn} and
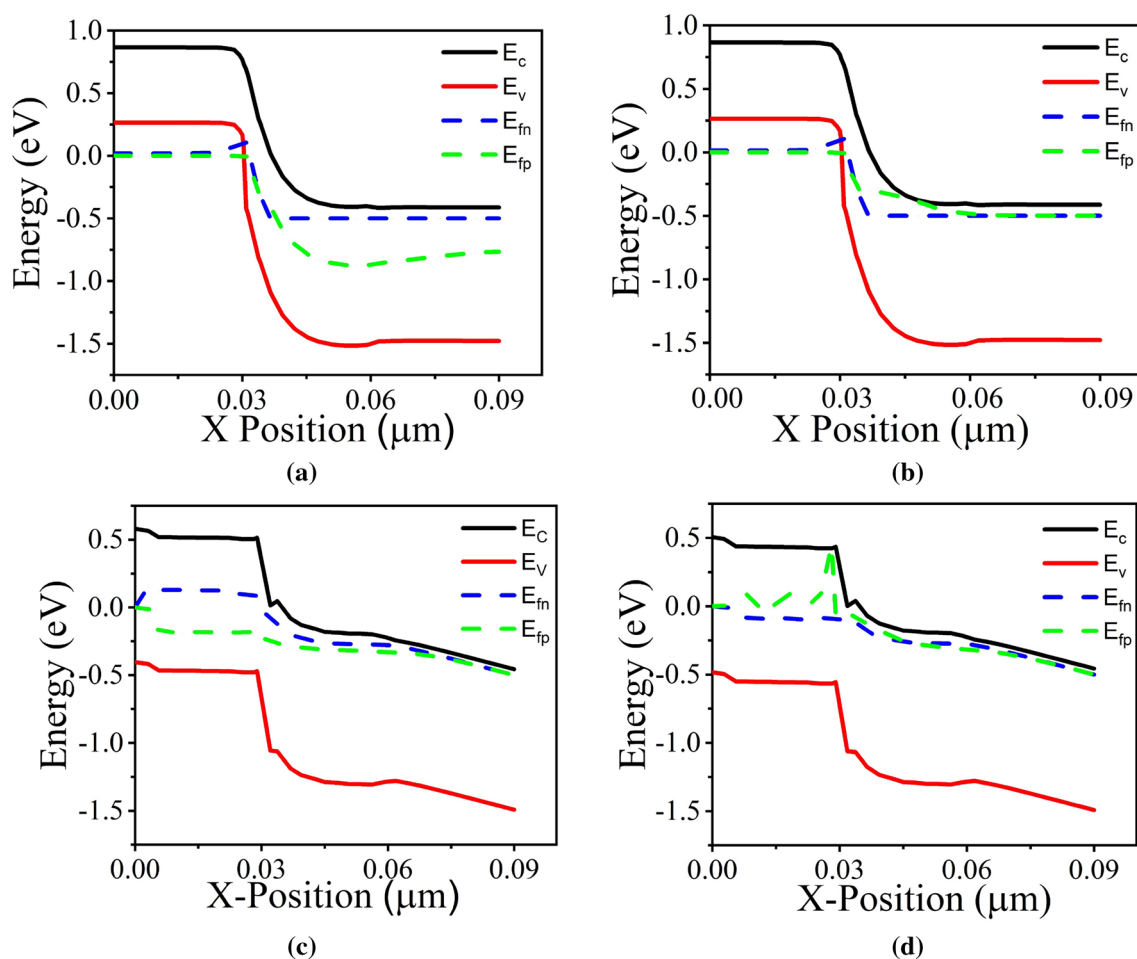
Fig. 5 Energy band diagram at constant $I = 0.7$ W/cm^2, $\lambda = 500$ nm for (a) HS-TFET photodiode in light, (b) HS-TFET photodiode in the dark, (c) ZHP-TFET photodiode in light, and (d) ZHP-TFET photodiode in the dark at $V_{DS} = 0.5$ V and $V_{GS} = 1.5$ V.

E_{fp} increases under the illumination area in the ON state ($V_{GS} = 1.5$ V, $V_{DS} = 0.5$ V). However, since there is no light production inside the channel under dark conditions, E_{fn} and E_{fp} will remain in synchrony, as illustrated in Fig. 5b and d. A significant difference between E_{fn} and E_{fp} is visualized in the HS-TFET photodiode compared to the ZHP-TFET photodiode in the illumination state. This indicates that the optical potential of the ZHP-TFET is lower than that of the HS-TFET.

The corresponding contour plot of the BTBT rate along the channel under dark and light states for both devices is shown in Fig. 6. It can be seen that the BTBT rate is lower in the dark state than in the illumination state for both photodiodes, and this is due to the presence of fewer charge carriers inside the illumination window under the dark condition relative to the illuminated state. The presence of a high-k oxide (HfO$_2$) layer above the source region enhanced the tunneling probability of charge carriers from the source to channel region.[6] Thus, it is evident from Fig. 6 that the ZHP-TFET exhibits tunneling rates on the order of 10^{31} and

7.3×10^{29} (cm^{-3} s^{-1}) during illuminated and dark conditions, respectively. In the case of the HS-TFET, the observed tunneling rates are around 10^{30} and 7×10^{29} (cm^{-3} s^{-1}) under light and dark conditions, respectively. Therefore, the BTBT rate of the ZHP-TFET photodiode is higher than that of the HS-TFET photodiode in both states.

The electron density profile for the TFET-based photodiodes under light and dark conditions is shown in Fig. 7. Both photodiodes have increased electron density under the light condition, as shown in Fig. 7b and d, which is due to the increased generation of optical carriers inside the illumination window. Furthermore, Fig. 7a and c shows lower electron density under dark conditions for both photodiodes. The ZHP-TFET photodiode also demonstrates increased electron density for both dark and light states, which indicates that it can be used for advanced optical sensors.

Strain in a heterojunction alters the atomic properties, thereby modulating the electrical characteristics of semiconductor devices. The proposed HS-TFET-based photodiode structure exhibits a stack of Si and Ge at the source region;
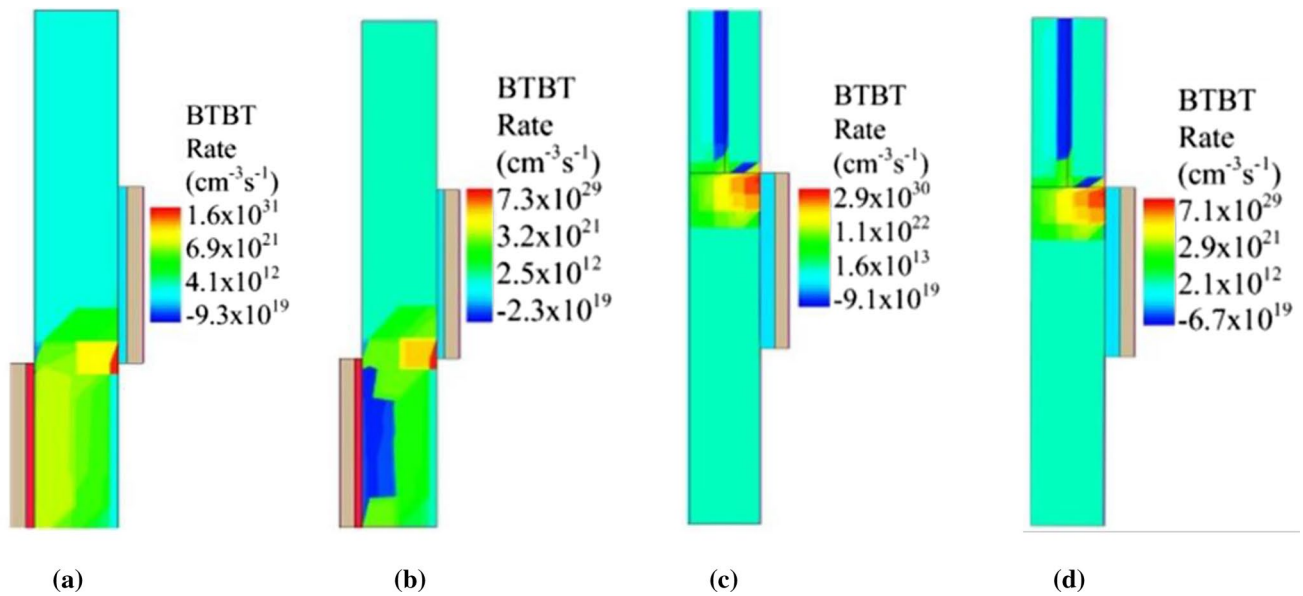
Fig. 6 BTBT rate of the ZHP-TFET photodiode under (a) illumination and (b) dark states, and HS-TFET photodiode under (c) illumination and (d) dark states at constant $I=0.7$ W/cm^2, $\lambda=500$ nm at $V_{DS}=0.5$ V.
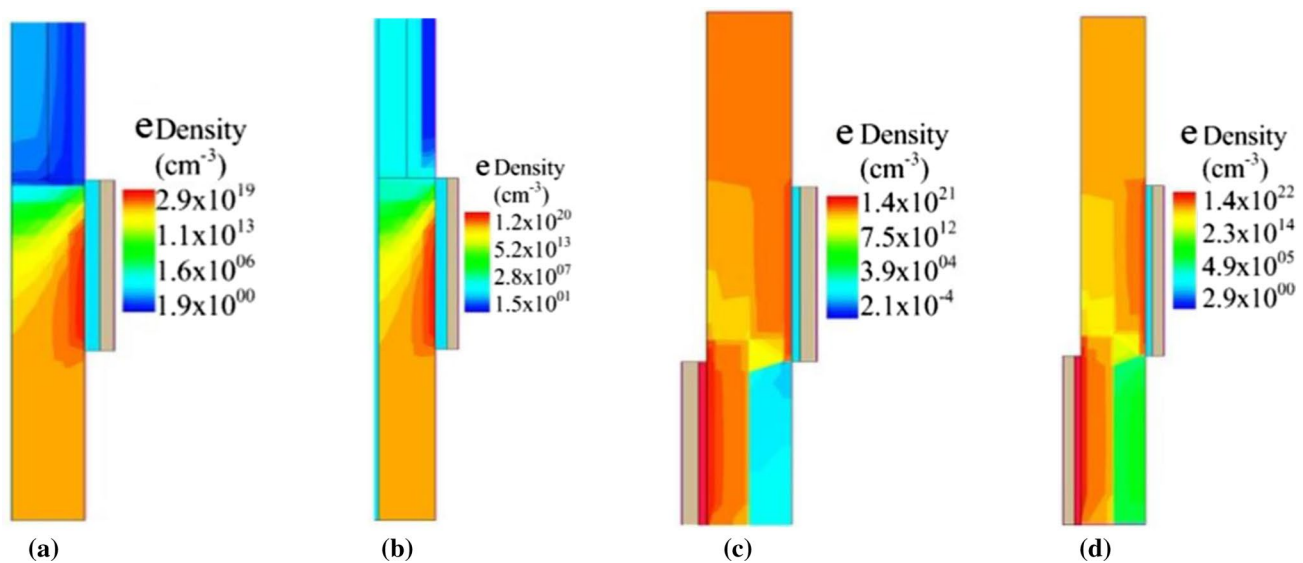

Fig. 7 Density of HS-TFET photodiode under (a) dark and (b) illumination states, and ZHP-TFET photodiode under (c) dark and (d) illumination states at constant $I=0.7$ W/cm^2, 500 nm $=\lambda$ and $V_{DS}=0.5$ V.

therefore, a uniaxial strain is introduced at the Si/Ge interface due to lattice mismatch.[12] Furthermore, the effect of strain in the source side of the HS-TFET is highlighted by considering its distribution along the XX-, YY-, and XY-axis of the device. This strain distribution includes the analytical profile placement (APP) strain, analytical profile distribution (APD) strain, and rectangular evaluation window (REW) strain model, as shown in Fig. 8. The presence of strain between the junctions also affects the electronic properties of the HS-TFET by modulating the electronic state and energy

bandgap of the heterojunction. Strain results in the variation in the electronic state of the device by narrowing the bandgap, as shown in Fig. 9. The presence of strain on the Si/Ge junction increases the electron affinity and decreases the conduction band energy relative to the unstrained effect, as summarized in Fig. 10.

In earlier analysis, it was found that the number of charge carriers is increased inside the illumination window when a device is illuminated. Consequently, the optical performance of such photodiodes is drastically improved, and such device
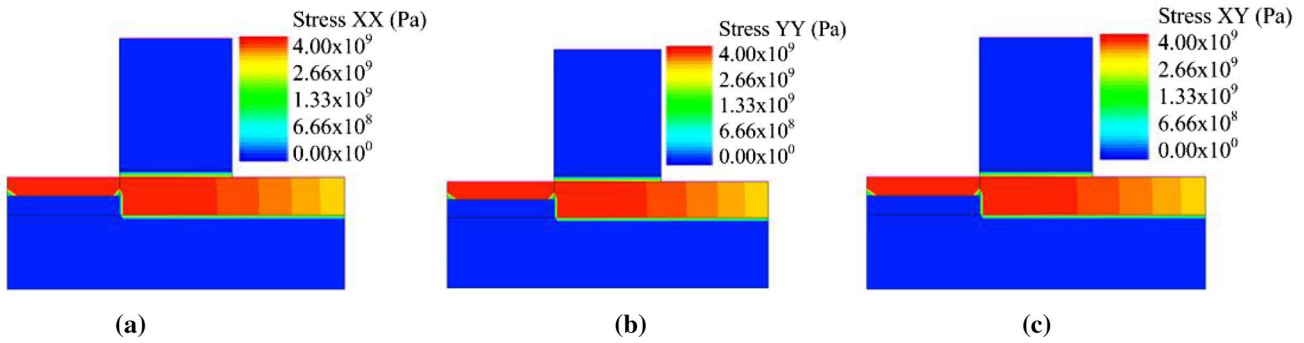
Fig. 8 TCAD Sentaurus-simulated device for stress distribution in a germanium–silicon HS-TFET: (a) XX component, (b) YY component, and (c) XY component at constant $I = 0.7$ W/cm^2, $\lambda = 500$ nm, and $V_{DS} = 0.5$ V.
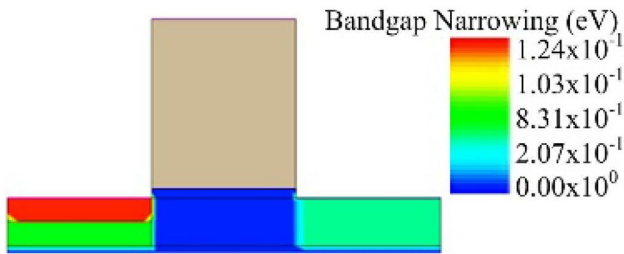

Fig. 9 Bandgap narrowing due to the strain effect in a silicon–germanium heterojunction of the hetero-stacked TFET photodiode.

Fig. 11 Transfer characteristics of ZHP- and HS-TFET-based photodiodes under dark and illumination conditions at constant $I = 0.7$ W/cm^2, 500 nm = λ, and $V_{DS} = 0.5$ V.
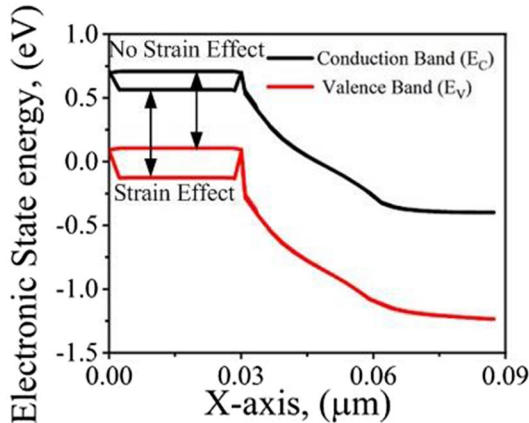

Fig. 10 Electronic state energy due to the strain effect in a silicon–germanium heterojunction of the hetero-stacked TFET photodiode.

can be used as a sensor. Figure 11 presents a comparison of the transfer characteristics between ZHP- and HS-TFET-based photodiodes. When the incidence angle of light is 0° in the TCAD simulator tool,[29] the light ray is incident normal to the photosensitive metallic surface in the +Y direction, and the device is considered to be in an illumination state. On the other hand, if we insert the angle of incidence equal to 90°, under this state the light ray moves parallel to
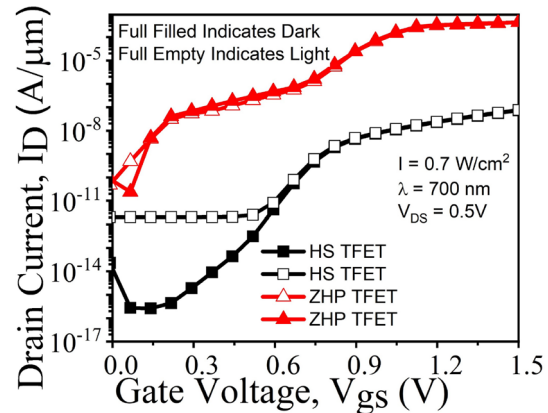
the photodiode in the +X-axis direction, and the device is considered to be in the dark state. Based on the angle of incidence, it is determined whether the photodiode is under light or dark mode. The ZHP-based TFET photodiode demonstrates improved drain current characteristics relative to the HS-TFET photodiode for both illumination and dark states. It is also observed that the ZHP-TFET photodiode exhibits lower variation in drain current (I_D) for both light and dark conditions. However, the HS-TFET photodiode shows a significant change in drain current due to an excess number of charge carriers created inside the optical area.

The considered photodiodes have a layered structure in the nanoscale regime; the electrostatic potential distribution of the HS- and ZHP-based TFET photodiodes along the Y-axis is shown in Fig. 12a and b, respectively. The HS-TFET photodiode exhibits greater change in the electrostatic potential (V) because of the major variation in drain current observed at a certain limit of gate voltage under light and dark states, while the ZHP-TFET photodiode has less variation in electrostatic potential due to negligible variation

in drain current observed in a certain small range of gate voltage (V_{gs}). The electrostatic potential curve will remain constant inside the metal, and beyond the metallic region the potential (V), it will decay exponentially with distance. When light is incident over the photosensitive surface, then optical voltage (V_{OP}) is induced across the metal oxide surface due to the generation of electron–hole pairs, which leads to exponential decay of net potential across the Y-axis of the device.

The spectral sensitivity (S_n)[32–34] of the photodiode is used to examine its optical performance and is determined by measuring the drain current at various wavelengths of light ranging from 400 nm to 700 nm. The S_n is mathematically expressed as

$$S_n = \frac{I_D(\lambda_1) - I_D(\lambda_2)}{I_D(\lambda_2)} \tag{8}$$

where $I_D(\lambda_1)$ and $I_D(\lambda_2)$ are the drain current at wavelength λ_1 and λ_2, respectively. The drain current tends to decrease when the wavelength is increased from λ_1 to λ_2.

The S_n as a function of λ for both TFET-based photodiodes is shown in Fig. 13a. It is seen that the S_n of the HS-TFET photodiode is about 221, whereas the S_n for the ZHP-TFET photodiode is 87.6 at a wavelength of 500 nm. Further, the S_n
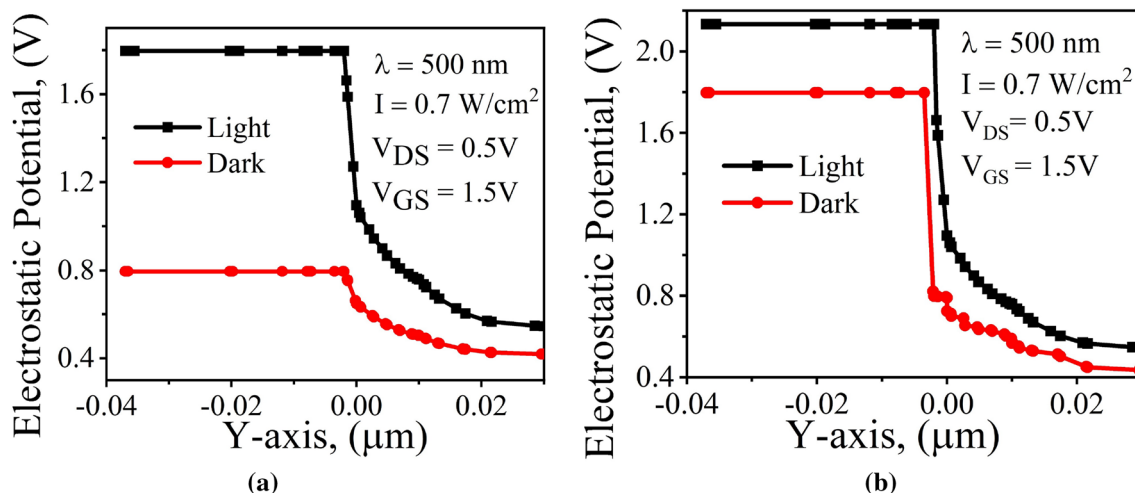

Fig. 12 Electrostatic potential distribution of (a) HS- and (b) ZHP-based TFET photodiodes along the Y-axis.
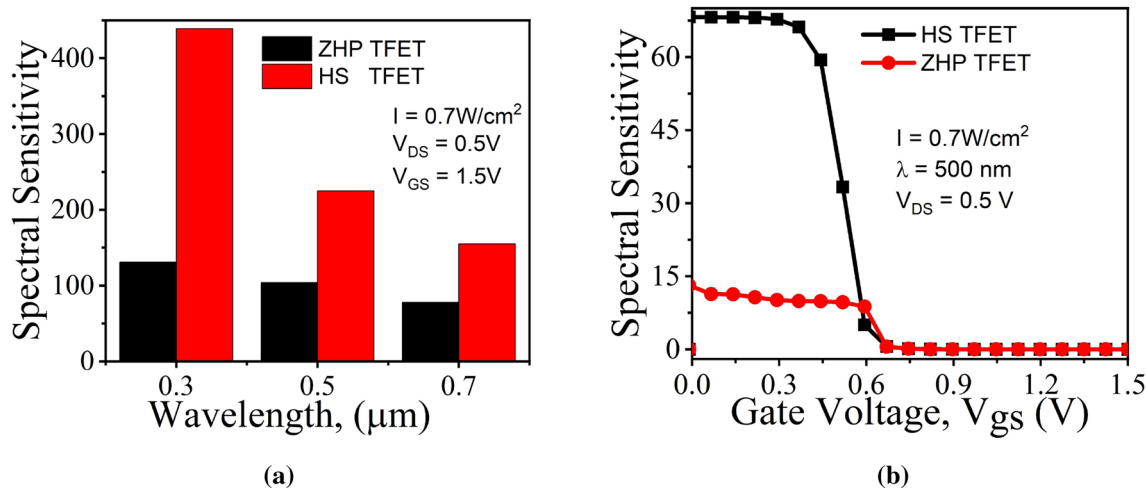

Fig. 13 Comparison of (a) spectral sensitivity (S_n) versus λ and (b) spectral sensitivity (S_n) versus V_{GS} of these photodiodes at $V_{DS} = 0.5$ V in the visible range (0.3–0.7) with $I = 0.7$ W/cm^2.
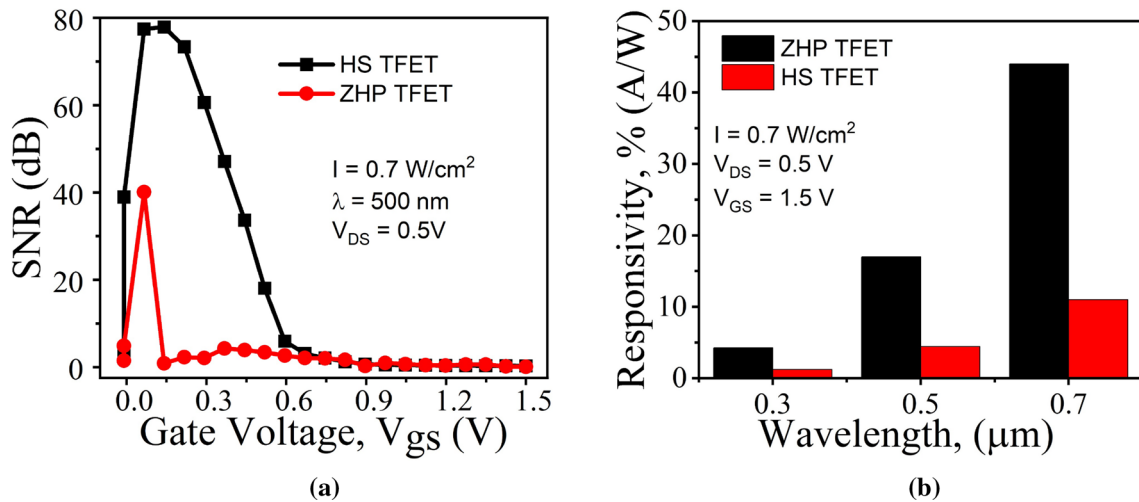
Fig. 14 Comparison of (a) SNR and (b) responsivity of the TFET-based photodiodes at constant intensity = 0.7 W/cm² of wavelength (0.3–0.7 μm) and V_{DS} = 0.5 V.
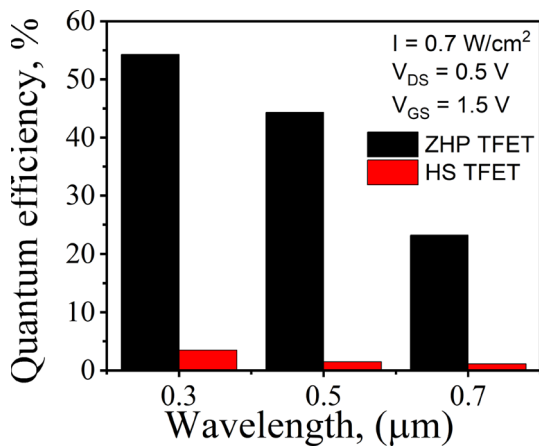

Fig. 15 Quantum efficiency plot of ZHP- and HS-TFET-based photodiodes at constant intensity = 0.7 W/cm² wavelength (0.3–0.7 μm) and V_{DS} = 0.5 V.

versus gate voltage for both TFET-based photodiodes is displayed in Fig. 13b. The drain current in the HS-TFET shows substantial fluctuations relative to the ZHP-TFET, which leads to greater sensitivity in the HS-TFET photodiode. The HS-TFET photodiode exhibits maximum sensitivity of 67.5 due to reduced variations in drain current during illumination. However, the ZHP-TFET photodiode exhibits an S_n value of 14.8 at lower V_{GS}.

The signal-to-noise ratio (SNR)[26] of the proposed photodiodes is shown in Fig. 14a. The SNR is defined as the ratio of photocurrent to dark current and is expressed as

$$SNR = 20\log\left(I_{\text{light}}/I_{\text{Dark}}\right) \tag{9}$$

It is seen from Fig. 14a that the SNR of the HS-TFET photodiode is around 79.3 dB, while the SNR of the ZHP-TFET photodiode is approximately 39.8 dB. The root cause of the improved SNR in the HS-TFET is the significant variation in the drain current observed at lower gate voltage. Thus, a higher SNR is detected for the HS-TFET-based photodiode than the ZHP-TFET photodiode.

Quantum efficiency (η)[33] is another essential element influencing the photodiode response. It is defined as the ratio of the number of electron–hole pairs formed to the number of incoming photons at a certain wavelength of light and is expressed as

$$\eta = \frac{\text{No of Electron hole pairs generated}}{\text{No of photons incident}} \tag{10}$$

We further compare the responsivity (R) of these photodiodes, as shown in Fig. 14b, which is expressed as[35–38]

$$R = \frac{q\eta\lambda}{hc} \tag{11}$$

where q represents the electron charge (= 1.6×10^{-19} C), c is the velocity of light (= 3×10^8 m/s) and h indicates the Planck constant (= 6.62×10^{-34} J s).

It can be seen from (11) that R is directly proportional to the quantum efficiency at a specific wavelength, and the rest of the parameters are constant. Figure 14b shows that the R of the ZHP-based TFET photodiode is significantly larger than that of the HS-TFET photodiode at various wavelengths.

Therefore, S_n and SNR of the HS-TFET photodiode are significantly higher in magnitude due to the maximum

Table II Quantum efficiency of various photodiodes

Photodiode	No. of electron–hole pairs generated	No. of incident photons	Quantum efficiency at wavelength $=0.5\ \mu m$, $I=0.7\ W/cm^2$, and $V_{DS}=0.5\ V$
ZHP-TFET	1.360×10^{21}	1.199×10^{22}	0.4434
HS-TFET	6.720×10^{20}	4.359×10^{22}	0.015

Table III Comparative analysis of considered photodiodes

Parameters	ZHP photodiode	HS photodiode
Spectral sensitivity (S_n)	14	67
I_{ON} (A/μm)	10^{-5}	10^{-7}
SNR (dB)	44	78
Responsivity (A/W)	0.17	0.04
BTBT ($cm^{-3}\ s^{-1}$)	10^{31}	10^{30}
Optical generation rate ($cm^{-3}\ s^{-1}$)	10^{23}	10^{22}
Quantum efficiency (η)	44.3%	1.5%

variation of drain current at lower V_{GS}. However, the number of optical charge carriers generated in the illumination window is significantly higher for the ZHP-TFET photodiode, which demonstrates higher R than the HS-TFET photodiode.

The quantum efficiency of both devices at different wavelengths is shown in Fig. 15. The photon energy is inversely proportional to the wavelength of incident light, and as the wavelength of incident light increases, fewer electron–hole pairs are generated inside the conductive channel. However, at a wavelength of 300 nm, the incident energy is sufficiently large to produce excess electron–hole pairs at the same intensity of light, thus resulting in higher quantum efficiency at a wavelength of 300 nm compared with higher wavelengths of light.

Table II shows the quantum efficiency of the demonstrated TFET-based photodiodes at a wavelength of 500 nm. The quantum efficiency of the ZHP-TFET-based photodiode is significantly higher than that of the HS-TFET-based photodiode, which is due to the excess number of carriers generated inside the illumination window of the ZHP-TFET-based photodiode.

Finally, we present a comparative study of the optical parameters between these photodiodes at a wavelength of 500 nm, as shown in Table III. It can be seen that the SNR and S_n are greater for the HS-TFET photodiode than the ZHP-TFET photodiode. This is due to large fluctuations in the charge carriers inside the illumination window in the HS-TFET photodiode, which points towards improved SNR and S_n. However, the ZHP-TFET photodiode seems to have improved I_{ON} current, better quantum efficiency, and faster responsivity, which is because of the greater photon absorption inside the light window in the ZHP-TFET photodiode.

Conclusion

In this paper, the optical characteristics of TFET-based photodiodes, namely HS-TFET and ZHP-TFET photodiodes, are investigated. The HS-TFET-based photodiode performs better in terms of SNR and sensitivity. However, other optical metrics including responsivity, quantum efficiency, optical generation, and BTBT rate are better in the ZHP-TFET-based photodiode. In the visible range of the spectrum, the optimum values of S_n and SNR observed for the HS-TFET-based photodiode are 67 dB and 78 dB, respectively, whereas the S_n and SNR are 14 dB and 44 dB, respectively, for the ZHP-TFET-based photodiode. Therefore, the TFET-based ZHP and HS photodiodes can be regarded as emerging optical devices in the visible range of the spectrum for photovoltaic applications.

References

1. S. L. Hurst, VLSI Custom microelectronics: digital: analog, and mixed-signal. *CRC Press*, (1998).
2. V. Sharma, S. Kumar, J. Talukdar, K. Mummaneni, and G. Rawat, Source pocket engineered hetero-gate dielectric SOI tunnel FET with improved performance. *Mater. Sci. Semicond. Process.* 143, 106541 (2010).
3. G.E. Moore, Cramming more components onto integrated circuits. *Electronics* 38, 114 (1965).
4. L. Menon, H. Yang, S. J. Cho, S. Mikael, Z. Ma, and W. Zhou, Transferred flexible three-color silicon membrane photodetector arrays. *IEEE Photon. Conf.* 342 (2014).
5. T. Someya, Y. Kato, S. lba, Y. Noguchi, T. Sekitani, H. Kawaguchi, and T. Sakurai, Integration of organic FETs with organic photodiodes for a large area, flexible, and lightweight sheet image scanners. *IEEE Tran. Electron Devices* 52, 2502 (2005).
6. S. Tiwari and R. Saha, Methods to reduce ambipolar current of various TFET structures: a review. *SILICON* 14, 6507 (2022).
7. J. Talukdar, G. Rawat, and K. Mummaneni, Analytical modelling and TCAD simulation for subthreshold characteristics of asymmetric tunnel FET. *Mater. Sci. Semicond. Process.* 142, 106482 (2022).
8. J. Talukdar, G. Rawat, and K. Mummaneni, Noise behavior and reliability analysis of non-uniform body tunnel FET with dual material source. *Microelectron. Reliab.* 131, 114510 (2022).

9. J. Talukdar, G. Rawat, and K. Mummaneni, Dielectric modulated single and double gate tunnel FET based biosensors for enhanced sensitivity. *IEEE Sens. J.* 21, 26566 (2021).

10. J. Talukdar, G. Rawat, and K. Mummaneni, Comparative analysis of the effects of trap charges on single- and double gate extended-source tunnel FET with δp^+ SiGe pocket layer. *J. Electron. Mater.* 49, 4333 (2020).

11. A.M. Walke, A. Vandooren, R. Rooyackers, D. Leonelli, A. Hikavyy, R. Loo, A.S. Verhuslt, K.H. Kao, C. Huyghebaert, G. Groesken, and V.R. Rao, Fabrication and analysis of a Si/Si$0_{0.55}$Ge$0_{0.45}$ heterojunction line tunnel FET. *IEEE Tran. Electron Devices* 61, 707 (2014).

12. K.R. Barman and S. Baishya, Silicon and germanium vertical super-thin body (VSTB) FET: a comparative performance overview including architectural stress-strain impact. *ECS J. Solid State Sci. Technol.* 11, 045007 (2022).

13. P.G. Der Agopian, J.A. Martino, A. Vandooren, R. Rooyackers, E. Simoen, A. Thean, and C. Claeys, Study of line-TFET analog performance comparing with other TFET and MOSFET architectures. *Solid State Electron* 128, 43 (2017).

14. S.W. Kim, W.Y. Choi, M.-C Sun, H.W. Kim, and B.G. Park, Design guideline of Si-based L-shaped tunneling field-effect transistors. *Jpn. J. Appl. Phys.* 51, (2012).

15. R. Saha, D.K. Panda, R. Goswami, B. Bhowmick, and S. Baishya, DC and RF/analog parameters in Ge-source split drain-ZHP-TFET: drain and pocket engineering technique. *Int. J. Numer. Modell.* 35, e2967 (2021).

16. R.M. Imenabadi, M. Saremi, and W.G. Vandenberghe, A Novel PNPN-like Z-shaped tunnel field- effect transistor with improved ambipolar behavior and RF performance. *IEEE Trans. Electron Devices* 64, 4752 (2017).

17. S. Sahoo, S. Dash, S.R. Routray, and G.P. Mishra, Impact of drain doping engineering on ambipolar and high frequency performance of ZHP line-TFET. *Semicond. Sci. Technol.* 35, 065003 (2020).

18. R. Saha, D. K. Panda, R. Goswami, B. Bhowmick, and S. Baishya, Effect of drain engineering on DC and RF characteristics in Ge-source SD-ZHP-TFET. in *Devices for Integrated Circuit (DevIC)*, (2021), p. 517–520.

19. S. Sahoo, S. Dash, S.R. Routray, and G.P. Mishra, A new Z-shaped gate line tunnel FET with improved electrostatic performance. *Iran. J. Sci. Technol. Trans. Electr. Eng.* 45, 1037 (2021).

20. S. Sahoo, S. Dash, S.R. Routray, and G.P. Mishra, Z-shaped gate TFET with horizontal pocket for improvement of electrostatic behavior. *Int. J. Numer. Modell. Electron. Netw. Dev. Fields* 34, 2808 (2020).

21. S. Gupta, Anju, and G. P. Mishra, Design and performance analysis of Z-shaped charge plasma TFET-based label-free biosensor. In *Devices for Integrated Circuit (DevIC),* (2021) p. 466–449.

22. S. Tiwari and R. Saha, DC and RF/analog performances of split source horizontal pocket and hetero stack TFETs considering interface trap charges: a simulation study. *Microelectron. Reliab.* 137, 114780 (2022).

23. K. Vanlalawmpuia and B. Bhowmick, Analysis of hetero-stacked source TFET and heterostructure vertical TFET as dielectrically modulated label-free biosensors. *IEEE Sens. J.* 22, 939 (2022).

24. A. Sikandar, M. Samiya, W. Liao, M.W. Iqbal, M. Ishfaq, K. Ramachandraiah, H. Muhammad, S. Ajmal, M.Z. Iqbal, A. Rehman, Z. Ahmed, S. Yousuf, H.M. Haque, and H.M.S. Ajmal, Switching photodiodes based on (2D/3D) PdSe$_2$/Si heterojunctions with a broadband spectral response. *J. Mater. Chem.* 9, 3998 (2021).

25. S. Joshi, P.K. Dubey, and B.K. Kaushik, Photosensor Based on split gate TMD TFET using photogating effect for visible light detection. *IEEE Sens. J.* 20, 6346 (2020).

26. W. Xu, L. Xiao, J. Li, and C. Zhang, Analysis and simulation of temperature characteristic of sensitivity for SOI lateral pin photodiode gated by transparent electrode, in: *Computer Engineering and Technology* 592, 173–182 (2015).

27. V. Kumari, M. Gupta, and M. Saxena, TCAD-based investigation of double gate junction less transistor for UV photodetector. *IEEE Trans. Electron Devices* 68, 2841 (2021).

28. S. Li, X. Chen, W. Ma, Z. Ding, C. Zhang, Z. Chang, X. He, Y. Shang, and Y. Zou, An innovative metal ions sensitive "test paper" based on virgin nanoporous silicon wafer: highly selective to copper (II). *Sci. Rep.* 6, 36654 (2016).

29. TCAD Sentaurus User Guide, Synopsys Inc., Mountain View, CA, USA (2020).

30. S.H. Kim, H. Kam, C. Hu, and T.-J. K. Liu, Ge-source tunnel field effect transistors with record high I_{ON}/I_{OFF}, VLSI Symp. Tech. Dig, 178 (2009).

31. H. Kao, A.S. Verhulst, W.G. Vandenberghe, B. Sorée, G. Groeseneken, and K. De Meyer, Direct and indirect band-to-band tunneling in germanium-based TFETs. *IEEE Trans. Electron. Devices* 59, 292 (2012).

32. V.D. Wangkheirakpam, B. Bhowmick, and P.D. Pukhrambam, Modeling and simulation of optically gated TFET for near infrared sensing applications and its low frequency noise analysis. *IEEE Sens. J.* 20, 9787 (2020).

33. S. Tiwari and R. Saha, Improved optical performance in near visible light detection photosensor based on TFET. *Microelectron. J.* 129, 105554 (2022).

34. X. Guo, Q. Liu, H. Zhou, X. Luan, C. Li, Z. Hu, A. Hu, and X. He, High-responsivity Si photodiodes at 1060 nm in standard CMOS technology. *IEEE Electron Device Lett.* 39, 228 (2018).

35. Y.R. Sipauba Carvalho da Silva, Y. Koda, S. Nasuno, R. Kuroda, and S. Sugawa, An ultraviolet radiation sensor using differential spectral response of silicon photodiodes. in *IEEE Sensors*, (2015), p. s1–s4

36. F. Djeffal and H. Ferhati, A new high-performance phototransistor design based on both surface texturization and graded gate doping engineering. *J. Comput. Electron.* 15, 301 (2016).

37. E.P. Mukhokosi, B. Roul, Saluru B. Krupanidhi, and K.K. Nanda, Toward a fast and highly responsive SnSe$_2$-based photodiode by exploiting the mobility of the coumter semiconductor. *ACS Appl. Mater. Interfaces* 11, 6184 (2019).

38. J. Zang, Z. Yang, X. Xie, M. Ren, Y. Shen, Z. Carson, O. Pfisier, A. Beling, and J.C. Camp, High quantum efficiency uni-traveling-carrier photodiode. *IEEE Photon. Technol. Lett.* 29, 302 (2017).